



Cite this: DOI: 10.1039/c8sm00128f

From jamming to collective cell migration through a boundary induced transition†

Oleksandr Chepizhko,^{ib ab} Maria Chiara Lionetti,^c Chiara Malinverno,^{de} Costanza Giampietro,^{ib f} Giorgio Scita,^{ib de} Stefano Zapperi^{ib *gh} and Caterina A. M. La Porta^{ib *c}

Cell monolayers provide an interesting example of active matter, exhibiting a phase transition from flowing to jammed states as they age. Here we report experiments and numerical simulations illustrating how a jammed cellular layer rapidly reverts to a flowing state after a wound. Quantitative comparison between experiments and simulations shows that cells change their self-propulsion and alignment strength so that the system crosses a phase transition line, which we characterize by finite-size scaling in an active particle model. This wound-induced unjamming transition is found to occur generically in epithelial, endothelial and cancer cells.

Received 17th January 2018,
 Accepted 20th April 2018

DOI: 10.1039/c8sm00128f

rsc.li/soft-matter-journal

1 Introduction

Understanding collective cell migration, when cells move as a cohesive and coordinated group is important to shed light on key aspects of embryogenesis, wound repair and cancer metastasis.¹ While cellular and multicellular dynamics and motility is controlled by a complex network of biochemical pathways,² it is becoming increasingly clear that a crucial role is also played by physical interactions among cells and between cells and their environment.^{3–7} Dense cellular assemblies, such as epithelial monolayers or cancer cell colonies, share many features with amorphous glassy materials, displaying slow relaxation,⁸ jamming⁹ and intermittent avalanche fluctuations.¹⁰ Cells can collectively flow like a fluid, but as cell proliferation increases cell density mutual crowding leads to

slowing down and arrest.^{8,9} The phenomenon of cell jamming could have a functional biological role, ensuring the development of tissue elasticity and protective barriers in epithelial tissues, providing also a suppressive mechanism for the aberrant growth of oncogenic clones.

The loss of motility in cellular assemblies shares similar features to the jamming transition observed in disordered materials such as colloids, granular media or foams.¹¹ As in disordered solids, cell jamming is thought to occur across different routes, either through the increase of cell density, or the reduction of the active forces responsible for cell motility.¹² In analogy with inanimate glassy systems, it seems reasonable to assume that jamming could also be produced by increasing intracellular adhesion, yet some experimental observations⁹ show that unjamming is associated with an increased adhesion, questioning the role of adhesion as a principal determinant of jamming (but see also ref. 13 for a different conclusion). Recent experiments also show that over-expression of the endocytic master regulator RAB5A leads to rapid fluidization and unjamming of a jammed confluent cell monolayer, due to polarization of cell protrusion and increase in traction force.¹⁴

Theoretical understanding of the cell jamming transition relies on simulations of vertex models,^{15–17} similar to those used for foam rheology^{18,19} but including self-propulsion, and of active particle models.^{20–30} In the Self Propelled Voronoi (SPV) model,¹⁷ space is subdivided into Voronoi polygons endowed with a mechanical energy due to cell surface tension, compression and adhesion. The polygonal structure then evolves according to equation of motion taking into account an active self-propulsion force and a noise term. Extensive numerical simulations yield a jamming transition and a possible phase diagram in terms of the main physical parameters encoded in the model.¹⁷ In this way, it is possible to identify physical determinants for jamming,

^a Institut für Theoretische Physik, Leopold-Franzens-Universität Innsbruck, Technikerstrasse 21a, A-6020 Innsbruck, Austria

^b Department of Applied Physics, Aalto University, P.O. Box 11100, FIN-00076 Aalto, Espoo, Finland

^c Center for Complexity and Biosystems, Department of Environmental Science and Policy, University of Milan, via Celoria 26, 20133 Milano, Italy.
 E-mail: caterina.laporta@unimi.it

^d IFOM, the FIRC Institute of Molecular Oncology, Via Adamello 16, 20139 Milano, Italy

^e Dipartimento di Scienze della Salute, San Paolo, University of Milan, 20122 Milano, Italy

^f Laboratory of Thermodynamics in Emerging Technologies, Department of Mechanical and Process Engineering, ETH Zurich, Sonneggstrasse 3, CH-8092, Zurich, Switzerland

^g Center for Complexity and Biosystems, Department of Physics, University of Milano, via Celoria 26, 20133 Milano, Italy. E-mail: stefano.zapperi@unimi.it

^h CNR – Consiglio Nazionale delle Ricerche, Istituto di Chimica della Materia Condensata e di Tecnologie per l'Energia, Via R. Cozzi 53, 20125 Milano, Italy

† Electronic supplementary information (ESI) available. See DOI: 10.1039/c8sm00128f

including the strength of the self-propulsion force and the shape anisotropy of the cell, determined by the ratio between the cell area and its squared perimeter.^{9,17} While cell jamming is typically observed experimentally by following in time the evolution of a cell monolayer in a confined space, collective cell migration is mostly observed and quantified in wound healing assays where cells are allowed to invade an empty space.^{3-7,21,23,24} The implementation of most vertex and Voronoi models relies on periodic boundary conditions (but see ref. 31 for recent improvements) and are thus not used to study wound healing, whose statistical features are often described by active particle models.^{10,20,23,32}

In this paper, we analyze the response of a jammed cell monolayer to the appearance of a wound, which creates empty space for the cells at the boundary. To this end, we analyze a large set of time-lapse images of cell layers using different cell types and experimental treatment, under confluent and wound healing conditions, and compare the results with simulations of an active particle model. We show that the model is able to quantitatively describe experimentally measured velocity distributions with open but also with confined boundary conditions. The model allows for a systematic investigation of the role of each relevant physical parameter so that we can place each experiment into a suitable phase diagram. Our simulations show that the model exhibits a clear jamming transition characterized by finite-size scaling. When we compare wound healing with confined experiments, we find that the latter are described by a set of physical parameters that place the system into the jamming phase, while the former fall into the flowing phase. Hence, the presence of a wound re-awakens jammed cells in a way similar to the effect of the overexpression of the endocytic regulator RAB5A.¹⁴

2 Methods

2.1 Cell culture

HeLa cell line (ATCC CCL-2) is cultured as discussed in ref. 10. Cells are seeded in bovine soluble collagen, or fibrillar bovine collagen or without collagen-coated dishes and grown up to reach confluence overnight (see ref. 10). Endothelial cells derived from embryonic stem cells with homozygous null mutation of the VE-cadherin gene (VEC null).³³ The wild type form of VE-cadherin was introduced in these cells (VEC positive) as described in detail in ref. 34. Endothelial cells isolated from lungs of wild type adult mice and cultured as previously described.^{10,35} The MCF-10A cell line is a non-tumorigenic human mammary epithelial cell line cultured as previously described.¹⁴ We also consider the same cells under RAB5A overexpression.¹⁴

2.2 Wound healing assay

For the migration assay, a wound is introduced in the central area of the confluent cell sheet by using a pipette tip and the migration followed by time-lapse imaging. HeLa cells were stained with 10 μ M Cell tracker green CMFDA (Molecular Probes) in serum-free medium for 30 minutes and then the complete

medium was replaced. Mouse endothelial cell monolayers were wounded after an overnight starving, washed with PBS, and incubated at 37 °C in starving medium. MCF-10A cell monolayers were wounded after an O/N doxycycline induction, washed with PBS, and incubated at 37 °C in fresh media + doxycycline.

2.3 Time lapse imaging

For HeLa cells, time-lapse multifield experiments were performed using an automated inverted Zeiss Axiovert S100 TV2 microscope (Carl Zeiss Microimaging Inc., Thornwood, NY) with a chilled Hamamatsu CCD camera OrcaII-ER. Displacements of the sample and the image acquisition are computer-controlled using Oko-Vision software (from Oko-lab). This Microscope was equipped with a cage incubator designed to maintain all the required environmental conditions for cell culture all around the microscopy workstation, thus enabling to carry out prolonged observations on biological specimens. Cell Tracker and Phase contrast images were acquired with an A-Plan 10 \times (NA 0.25) objective; the typical delay between two successive images of the same field was set to 10 minutes for 12 hours. For mouse endothelial cells and MCF-10A cells, time-lapse imaging of cell migration was performed on an inverted microscope (Eclipse TE2000-E; Nikon) equipped with an incubation chamber (OKOLab) maintained at 37 °C in an atmosphere of 5% CO₂. Movies were acquired with a Cascade II 512 (Photometrics) charge-coupled device (CCD) camera controlled by MetaMorph Software (Universal Imaging) using a 4 \times or 10 magnification objective lens (Plan Fluor 10, NA 0.30). Images were acquired every 2 or 5 min over a 24 h period. See ref. 10 and 14 for more details.

2.4 Particle image velocimetry (PIV)

The measurements of the velocity field were done using PIVlab app for Matlab.³⁶ The method is based on the comparison of the intensity fields of two consequent photographs of cells. The difference in the intensity is converted into velocity field measured in px per frames and then converted to μ m h⁻¹.¹⁰

2.5 Model

We consider a model for interacting cells similar to the one introduced in ref. 23. Cells are treated as particles moving according to the following equation of motion:

$$\frac{d\mathbf{v}_i}{dt} = -\alpha\mathbf{v}_i + \sum_{j \in n.o.f.i} \left[\frac{\beta}{N_i} (\mathbf{v}_j - \mathbf{v}_i) + \mathbf{f}_{ij} \right] + \sigma\eta_i + \hat{\mathbf{v}}_i F_0. \quad (1)$$

The first term represents the dissipation processes and α is a damping parameter. The second term represents the interaction of i -th cell with the other cells. The interaction reflects the tendency of a particle to orient its velocity with the velocity of its neighbors, with a coupling strength β , and N_i is the number of neighbors of i -th cell.³⁷ The neighbors of each particle are defined in the same way as ref. 23: the neighborhood of a particle i is split into 6 equal sectors and the particle closest to the particle i in each sector (within the interaction radius of 100 μ m) is chosen to be a neighbor. The second

interaction term, \mathbf{f}_{ij} , represents the short-range hard-core repulsion and long-range attraction, and has the form

$$\mathbf{f}_{ij} = -\nabla_i U(r_{ij}), \quad (2)$$

where

$$U(r) = U_0 \exp(-(r/a_0)^2) + U_1(r - a_1)^2 H(r - a_1), \quad (3)$$

where $H(x)$ is the Heaviside function $H(x) = 1$ for $x > 0$ and $H(x) = 0$ otherwise. The motion of a cell is affected by a noise term $\sigma_0 \eta_i$, where η_i is an Ornstein-Uhlenbeck process with correlation time τ :

$$\tau \frac{d\eta_i}{dt} = -\eta_i + \zeta_i, \quad (4)$$

where ζ_i is a Gaussian random vector, with zero mean, unit variance and correlations $\langle \zeta_i(t) \zeta_j(t') \rangle = \delta_{ij} \delta(t - t')$. Finally, we consider an additional active force directed along the cell velocity $\hat{\mathbf{v}}_i$ and with intensity F_0 . We notice that both η_i and $F_0 \hat{\mathbf{v}}_i$ act as self-propulsion forces.^{38–40} Yet, both terms are needed in the model to reproduce experiments, otherwise it is not possible to disentangle the average active force from its fluctuations.

As in the original model,²³ the free surface is modeled by surface particles, that are hindering cells invade the space. The interaction between a surface particle and a cell is modeled by:

$$\mathbf{f}_{ij}^s = -\nabla_i U^s(r_{ij}), \quad (5)$$

where $U^s(r)$ is $U^s(r) = A_s \exp(-(r/a_s)^2)$. With each surface particle a scalar damage variable q is associated, and it is chosen to obey:

$$\nu \frac{dq_i}{dt} = \sum_{j: \mathbf{r}_j \in S_i} |\mathbf{f}_{ij}^s|. \quad (6)$$

The surface particle disappears if the damage variable reaches its critical value $q_i = q_c$. To simulate wound healing conditions, we place the cell in a box of size $2L \times L$ in which we place cells surrounded by surface particles. We first do not allow damage on the surface particles and let the system relax for a time $T/4$. We then allow surface particles to be damaged so that the wound healing process starts. We first let the front evolve for an additional time $T/4$ and finally collect velocity statistics for a time $T/2$. This procedure allows to minimize transient effects. The model can also be simulated in confluent conditions by setting the damage variable to $q_c = \infty$, so that the cells never invade the surrounding space.

Some model parameters are held fixed throughout all the simulations: $r_s = 50 \mu\text{m}$, $\nu = 7 \text{ h}^{-1}$, $A_s = 2400 \mu\text{m}^2 \text{ h}^{-2}$, $a_s = 8 \mu\text{m}$, $q_c = 30 \mu\text{m}$, $\tau = 1.39 \text{ h}^{-1}$, $U_0 = 2400 \mu\text{m}^2 \text{ h}^{-2}$, $U_1 = 2 \text{ h}^{-2}$, $a_1 = 35 \mu\text{m}$. Other parameters are varied and reported using the following units: $[L] = \mu\text{m}$, $[\alpha] = \text{h}^{-1}$, $[\beta] = \text{h}^{-1}$, $[\sigma_0] = \mu\text{m} \text{ h}^{-3/2}$, $[F_0] = \mu\text{m} \text{ h}^{-2}$.

2.6 Fit of the experimental data

To find the values of simulation parameters that fit experimental data, extensive numerical simulations were performed to cover the parameter space. For both simulations and experiments, we discard the initial transient frames and perform all the analysis for times

$T/2 < t < T$, where T is the total duration of the experiment. The main parameters to vary were the alignment strength β , the noise intensity σ_0 , the self-propulsion force F_0 , and, to less extent, the damping coefficient α . Then the fitting was done minimizing the variable $M = ((\zeta_{\text{exp}} - \zeta_{\text{sim}})/\zeta_{\text{exp}})^2 + \int d\mathbf{v} (P_{\text{exp}}(\mathbf{v}) - P_{\text{sim}}(\mathbf{v}))^2 / \Sigma_{\text{exp}}$,²³ where ζ_{exp} and ζ_{sim} are correlation lengths in experiments and simulations, while $P_{\text{exp}}(\mathbf{v})$ and $P_{\text{sim}}(\mathbf{v})$ and the respective velocity distributions. The variable M was computed for a large number of simulations spanning the parameter space and its minimum was selected as the best fit (see Table S1, ESI†).

3 Results

3.1 Experimental measurements of velocity distributions and correlations

We consider time lapse images recorded during wound healing assays performed for a variety of cell lines under different experimental conditions (see Section 2 for detailed information): HeLa cells on different substrates: plastic, soluble collagen, or fibrillar collagen (see ref. 10); endothelial cells derived from embryonic stem cells with homozygous null mutation of the VE-cadherin gene (VEC null)³³ and those with the corresponding wild type form of VE-cadherin (VEC positive);³⁴ Endothelial cells isolated from lungs of wild type adult mice (lung ECs);^{10,35} A non-tumorigenic human mammary epithelial cell line (MCF-10A) with the over-expression of RAB5A, known to induce unjamming, and the corresponding wild type (WT) cells.¹⁴ As a comparison, we also analyze HeLa cells and MCF-10A cells in confluent conditions without inducing wound healing.

We analyze all the experimental time lapse images using particle image velocimetry (PIV) which allows us to estimate the local velocity field inside the cell sheet (see Fig. 1a) and the corresponding velocity distributions.¹⁰ In particular, we measure the distribution of the velocity absolute values $P(v)$ (see Fig. 1b), the distribution of the velocity orientations (see Fig. 1c) and the velocity-velocity correlation lengths ζ from an exponential fit of the correlation functions (see Fig. 1d). It is interesting to notice that correlations lengths obtained from MCF-10A cells under different conditions scale linearly with the standard deviation of the velocity distribution $\Sigma = \sqrt{\langle (v_x^2 + v_y^2) \rangle - (\langle v_x \rangle)^2 - (\langle v_y \rangle)^2}$. This relation was predicted by a theoretical model of collective cell migration where it implies that the effective friction is dominated by cell-cell interactions over cell-substrate interactions.¹³

Considering all the experimental results, we obtain a set of 40 distributions for different cell lines and experimental conditions describing the statistical features of the velocity during collective cell migration. To visualize all the data in a simple way, in Fig. 2a we report the average velocity $\langle v_x \rangle$ perpendicular to the front as a function of Σ . The results show that the standard deviation of confluent systems is roughly one order of magnitude smaller than the one observed during wound healing for the same cells. Considering the wound healing case, we observe that MCF-10A cells move considerably faster than the other cells and, as expected, RAB5A overexpression leads to net increase in the average velocity with little changes in Σ .

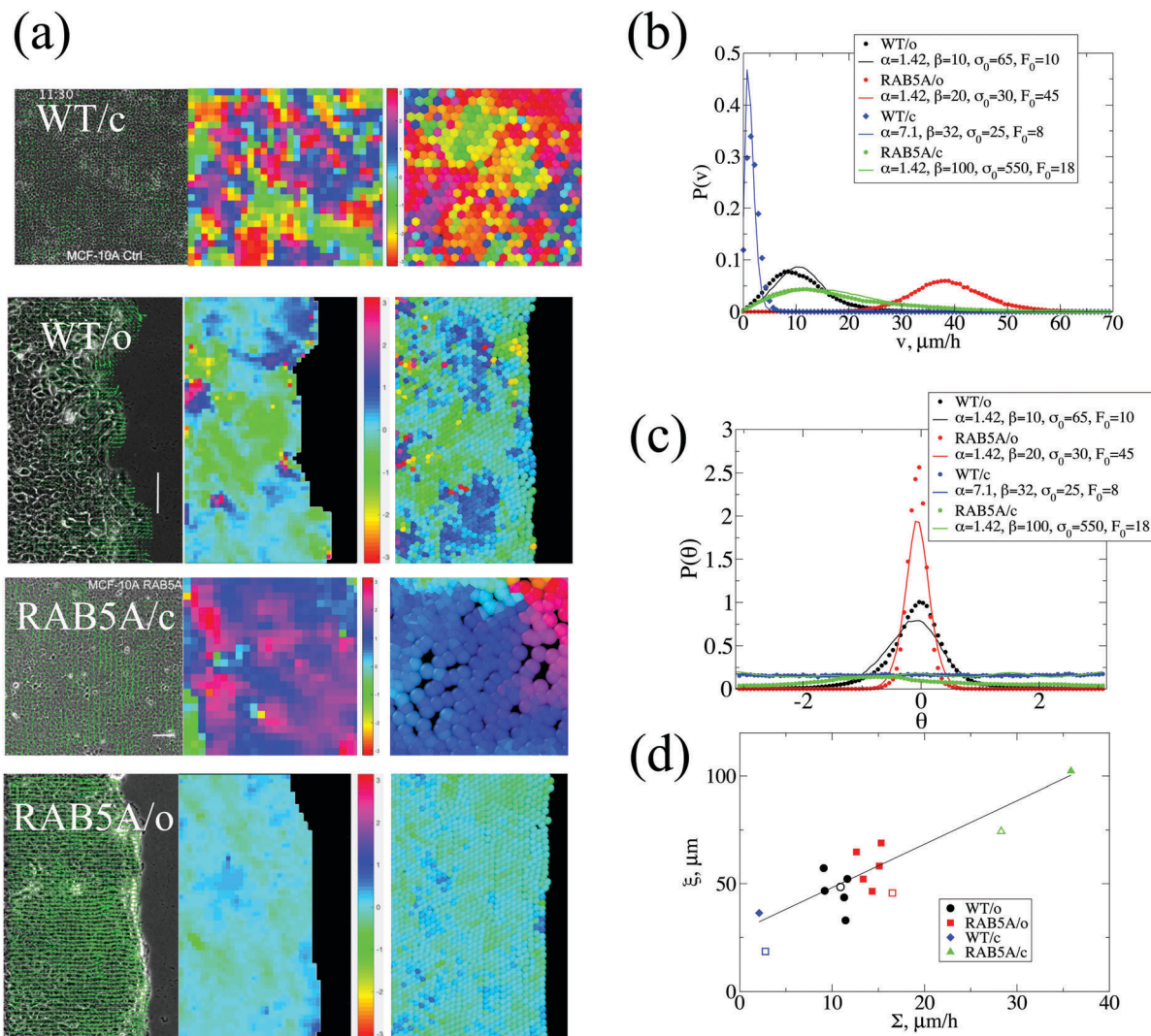


Fig. 1 Statistical properties of collective migration in epithelial cells. (a) Velocity maps obtained from PIV for WT MCF-10A cells in wound healing (WT/o) and confluent (WT/c) conditions, as well as MCF-10A cells with RAB5A overexpression under the same conditions (RAB5A/o and RAB5A/c), respectively (see also Supplementary videos, ESI†). Arrows represent the velocities and the color their orientations. Experimental results are compared with simulations. Simulations with open boundaries are performed with $N = 12\,000$ particles and those with closed boundaries with $N = 1\,000$ particles. (b) The distribution of the absolute values of the velocities for the experiments reported in panel (a) compared with the corresponding simulation results. (c) Distribution of velocity orientations for the same cases. (d) Velocity correlation length ξ_z as a function of the velocity fluctuations Σ . The observed correlation is consistent with the prediction of an earlier model.¹³

It is interesting to notice that cell velocities under wound healing conditions are typically larger than observed under confluent conditions. This change is, however, not instantaneous as illustrated in Fig. 3a and c. Velocities increase initially only in the wound region until an activity front propagates into the bulk, in agreement with previous findings.^{41–43} This transient propagation is also reflected by the velocity distribution that evolves until it reaches a steady-state (see Fig. 3b and d). As discussed in the Methods section, the analysis of the velocity distributions and correlations is always done excluding the initial transient regime.

3.2 Comparison of experimental velocity distributions with simulations

To compare the experiment with the model, we run a large set of simulations with both open and closed boundary conditions,

employing a cell density that corresponds to the one observed in experiments for confluent cell layers. We explore the parameter space defined by different values of $(F_0, \sigma_0, \beta, \alpha, U_1)$ and inspect how each parameter affects the velocity distributions (see Fig. 4). We observe that F_0 and α have a considerable effect on $\langle v_x \rangle$, while β and σ_0 have opposite effects on the velocity fluctuations: Σ increases with σ_0 and decreases with β . The adhesion strength is found to have little effect on the velocity distributions for the range we examined.

We find the best match between experiments and simulations (see Methods) and identify a set of four parameters $(F_0, \sigma_0, \beta, \alpha)$ that best describe each individual experiment. Representative examples of the good match between experiments and model are reported in Fig. 1 for the case of MCF-10A cells under different conditions. We have also checked that the simulations

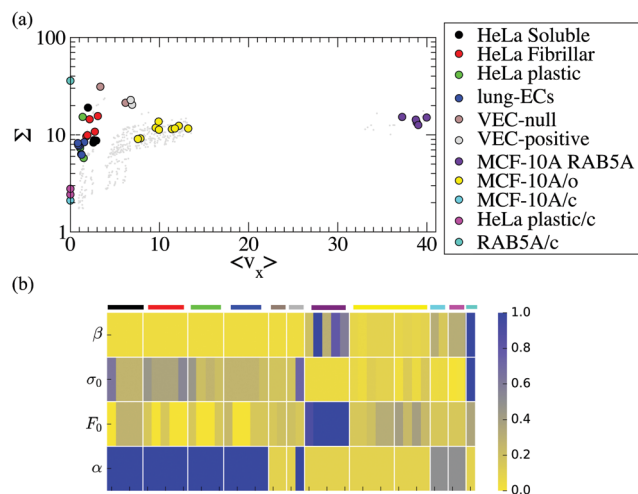


Fig. 2 The parameter space of cell migration. (a) A map of the average velocity in the invasion direction $\langle v_x \rangle$ and the velocity standard deviation Σ for all the cell lines analyzed. (b) A colormap of the best parameters β , F_0 , σ_0 and α obtained by comparing each experiment with simulations. The color scale is normalized separately for each parameter (with $\beta^{\max} = 100$, $F_0^{\max} = 50$ and $\sigma_0^{\max} = 400$ and $\alpha^{\max} = 14.2$). Each column represents an experiment with a cell line associated with the color legend.

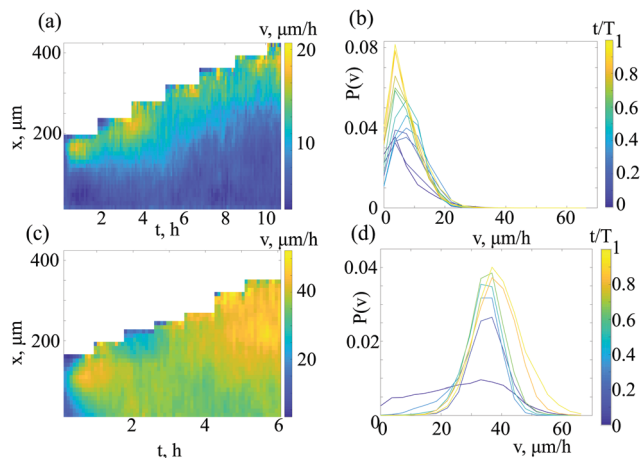


Fig. 3 The spatio-temporal dynamics of wound healing. The color-maps in panels (a) and (c) display the average velocity of obtained from PIV average over y (the direction parallel to the front) as a function of x and time. The corresponding velocity distribution at different times are reported in panels (b) and (d). Results for WT MCF-10A cells are reported in panels (a) and (b) and for MCF-10A cells under RAB5A overexpression in panels (c) and (d).

reproduce the value of the correlation length with reasonable accuracy. The collection of parameters obtained for all the experiments is summarized in Fig. 2b as normalized color maps. The map allows us to observe some general trends in the parameter space: in particular MCF10-A with RAB5A overexpression stand out for their higher value of self-propulsion (F_0) and mutual alignment (β) with respect to the other cells. Furthermore, MCF-10A, both WT and RAB5A, display weaker noise (σ_0) in comparison with the other cells.

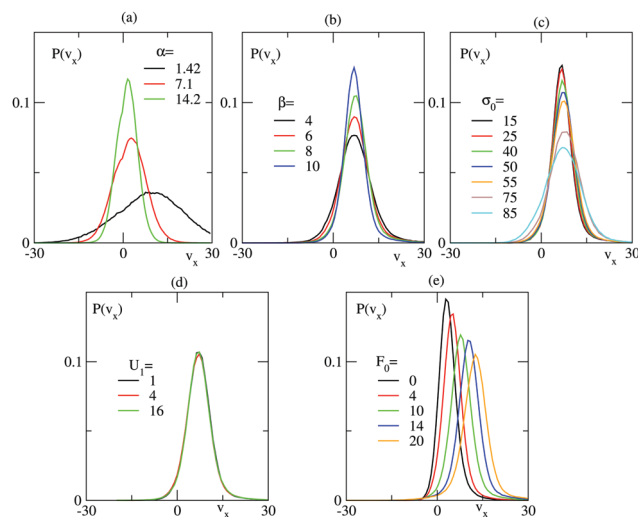


Fig. 4 Effect of the model parameters on the cell velocity distribution for a system with $N = 12000$ particles with open boundary conditions. Effect of (a) damping α , (b) alignment strength β , (c) noise σ_0 , (d) adhesion U_0 and (e) self-propulsion force F_0 on $P(v_x)$, where v_x is the velocity in the invasion direction.

3.3 Finite size scaling at the jamming transition

A simple inspection of the experimentally measured velocity distributions does not provide a clear understanding of the possible jamming or flowing behavior of the cell monolayers. Simulating the model, however, allows for a complete characterization of its dynamical behavior in terms of a reduced set of parameters. Following recent work,¹⁷ we analyze the mean-square displacement (MSD) of individual cells in simulations of confluent layers and study how it changes as key parameters are varied. For instance, Fig. 5a shows that the MSD is a linear function of time whose slope, the effective diffusion constant D , increases with noise parameter σ_0 . A sharp increase in D is usually associated with a transition from a jamming to a flowing state. In our case, Fig. 5b shows that D depends on σ_0 in a system-size dependent manner. This is generally expected for phase transitions in and out of equilibrium, where finite size scaling governs the behavior of the system near the critical point. We thus propose a finite-size scaling form for the noise and size dependence of the diffusion constant

$$D(\sigma_0, N) = f((\sigma_0 - \sigma_c)N^{1/\nu}) \quad (7)$$

where the scaling function $f(x) \propto x^\gamma$ for $x > 0$ and $f(x) = \text{const.}$ for $x < 0$. The data collapse reported in Fig. 5c according to eqn (7) indicates that $1/\nu = 0.5$ and $\gamma = 0.85$. A similar finite-size scaling collapse can be done in dependence on F_0 : $D(F_0, N) = g((F_0 - F_c)N^{1/\nu'})$, with $g(x) \propto x^{\gamma'}$ for $x > 0$ (see Fig. 6), yielding $1/\nu' = 0.5$ and $\gamma' = 1.3$.

3.4 Wound healing and unjamming

Collecting together all the simulations performed, we construct a phase diagram distinguishing the jammed from the flowing state as a function of F_0 and σ_0 , as reported in Fig. 7. Here for practical reasons, we have concentrated on fixed values for $\beta = 10$ and $\alpha = 1.4$ that correspond to a large set of experimental data. It would be possible in principle to reconstruct the whole

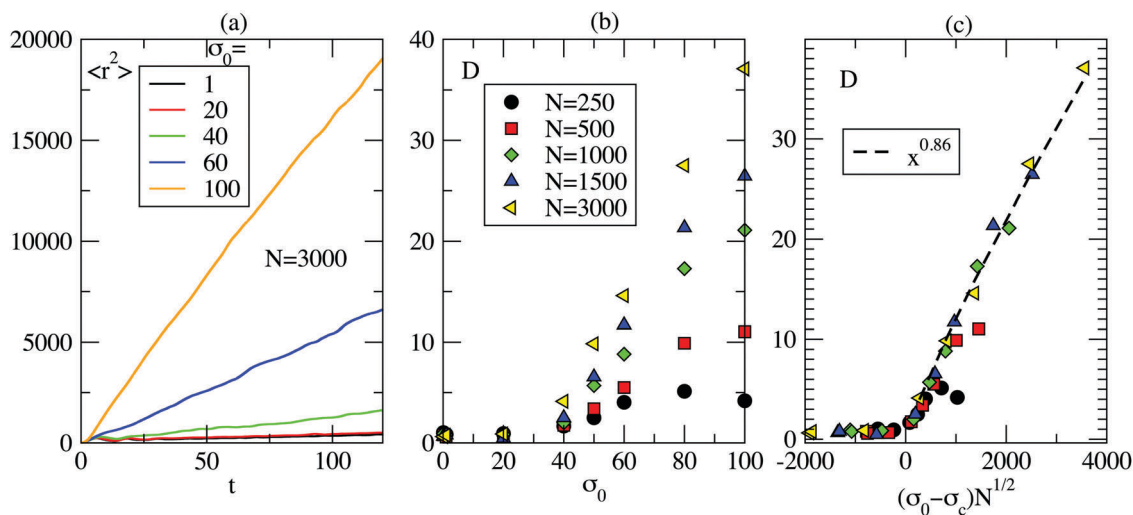


Fig. 5 Characterization of the jamming-flowing transition in a simulated confluent layer. (a) The time dependence of the mean-square displacement as a function of the noise amplitude σ_0 (b) the diffusion constant displays a system-size dependent behavior above a noise level σ_c that can be used to identify the jamming point. (c) The curves from panel (b) can be collapsed assuming a finite-size scaling form.

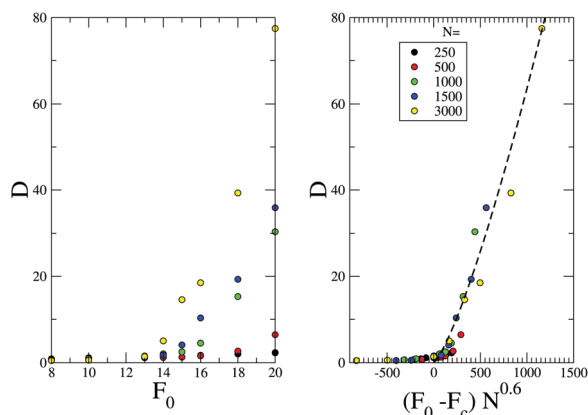


Fig. 6 (a) The diffusion constant as a function of the self-propulsion force F_0 displays a system-size dependent behavior above a noise level F_c that can be used to identify the jamming point. (b) The curves from panel (a) can be collapsed assuming a finite-size scaling form.

4-dimensional phase diagram but this is extremely demanding computationally.

We are now in position to reach the goal posed at the beginning of this paper and identify the phase for each experimental sample. To this end, we report in Fig. 7 all the parameter values (F_0, σ_0) extracted from the experimental measurement (see Table S1 (ESI[†]) for the list of all fitted parameters). The general trend we observe from the figure is that all the experiments performed in confluent layers fall into the jammed phase, while almost all of the wound healing experiments are in the flowing phase. Notice that here we are projecting all the data into the $(\beta = 10, \alpha = 1.42)$ plane so discrepancies could also arise due to the fact that experimental data are described by different values of β and α .

Taken together our results suggest that when a jammed confluent layer is perturbed by wound healing, providing additional space for the cells, the system undergoes a phase transition to the

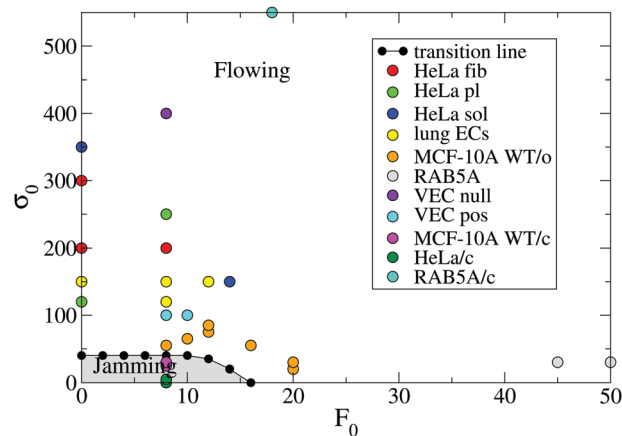


Fig. 7 The jamming phase diagram. A projection of the jamming phase diagram on the (σ_0, F_0) plane, for $\beta = 10$ and $\alpha = 1.4$. For each experiment, we report on the phase diagram the best estimate for σ_0 and F_0 . Experiments performed in confluent conditions are all in the jamming phase, those in wound healing conditions are mostly in the flowing phase.

flowing state. This is reflected by the fact that key parameters describing self-propulsion, noise or alignment change their values, implying that the monolayer responds in an active way to the change of boundary conditions. We checked that this process is not an artifact of the model or the fitting by considering wound healing before and after closure. Results show that it is not possible to fit the velocity distributions before and after healing with the same parameters, as illustrated in Fig. 8. It is only some time after closure that the cell layer slowly falls back into the jammed state.

4 Discussion

Soft and glassy materials are known to undergo a jamming transition, characterized by limited mobility and slow relaxation

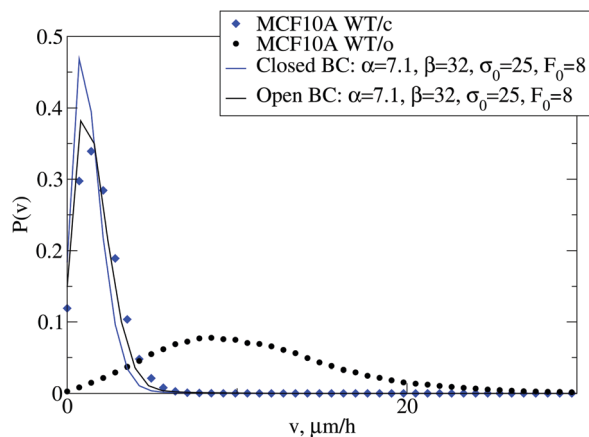


Fig. 8 Wound healing involves a change of internal parameters. Velocity distribution for WT MCF-10A cells measured in confluent conditions and after wound healing. We also report the distribution obtained fitting the confluent data with the model under closed boundary conditions. When the same parameter are used to simulate the cells with open boundary conditions the resulting velocity distribution is very similar to the one obtained with closed boundary conditions and does not match the experiments. This indicates that parameters are changed in response to the wound.

upon fine tuning of a set of physical control parameters including density, temperature and shear stress.¹¹ Dense cellular assemblies such as epithelial tissues and cancer are recently emerging as paradigmatic examples of jamming in active matter,^{9,13,44} a well studied non-equilibrium state of matter where an internal force drives each of the elementary units of the system. Examples of active matter range from artificial self-propelled colloidal particles, to bacteria, epithelial and cancer cells or even large groups of animals such as fish schools or birds flocks. A key issue for active matter is to understand what are the main physical determinants for jamming, which would play a role analogous to stress, density and temperature in conventional matter.

Current understanding of the jamming transition in cellular systems relies mostly from vertex models¹⁵ and SVP models,^{16,17} which allow to clarify the role of many key biophysical parameters, such as cell anisotropies and self-propulsion strength. These models, however, are defined for systems with periodic boundary conditions and are therefore not appropriate to study the response of jammed epithelia to a wound, a well studied protocol to understand and quantify collective cell migration in epithelial and cancer cells.^{3–7,10,21,23,24} Active particle models have proven very effective to quantitatively describe wound healing^{10,23,32} and jamming,^{22,25–30} but the connection between the two phenomena has not been widely explored. In the paper, we fill this gap by a combination of experiments and numerical simulations.

We analyze a large set of time-lapse experiments of cellular assemblies performed for different cell lines both in confluent conditions or after wound healing. In all these case, we compute the velocity distributions by PIV and study how the distribution changes in presence of a wound. We start our analysis from the MCF-10A cell line that was recently shown to undergo a transition from a jammed to a flowing state by

over-expression of RAB5A, a master regulator of endocytosis.¹⁴ Here we compare this transition with the similar fluidization induced by a wound. To obtain a quantitative characterization of the transition, we compare the experimental results with numerical simulations of an active particle model. In this way, we obtain the model parameters that best describe the experimentally measured velocity distributions. These parameters describe the self-propulsion force, the alignment interactions, intracellular adhesion, damping and noise and allow for a physical characterization of different cell lines and experimental conditions.

Our first observation is that the internal parameters typically change when a wound is present. This is a typical feature of living matter and not shared by ordinary inanimate matter where boundary conditions are not expected to influence the internal parameters of the system. Thus a jammed solid could possibly slowly invade a new open space and unjamming would eventually only occur because of a reduction of the density. In our case, however, the change of velocity distribution is instead compatible with a rapid change of internal parameters such as self-propulsion or alignment, way before the cell density is reduced. This result is consistent with the recent theoretical observation, made in the context of active particle models, that an increase in particle activity corresponds to a fluidization of the system.⁴⁵

Once the parameters associated to each experiment have been determined, we are able to place them on a phase diagram reconstructed with the model. To this end, we perform numerical simulations of the active particle model under closed boundary conditions. The jamming phase can be identified considering the particle diffusion, quantified by the mean-square displacement.¹⁷ We observe that the effective diffusion constant displays system size dependent effect in parameter space, allowing us to identify the transition point. As expected for second-order phase transitions, the curve describing the variation of the diffusion constant with control parameters and system size obeys finite size scaling. We can thus obtain scaling exponents by performing data collapse.

In our analysis of wound healing experiments, we have recorded parameters in steady-state conditions, disregarding the initial transient phase where the horizontal velocity builds up. Previous studies have shown that collective migration is associated with the propagation of waves of coordinated reorientation starting at the front.^{41–43} This is in line with our observation of a change of parameters induced by the boundary and suggests that changes first occur at the wound site and then rapidly propagate inside the layer. The phenomenon of collective cell velocity reorientation in the direction of the wound has been explained considering cell guidance through intracellular force propagation in combination with the idea of plithotaxis, defined as the tendency for cells to move along the axis of maximal normal stress.⁴⁶ The presence of a wound suddenly decreases the local stress on the boundary cells, inducing internal changes that are then transmitted to the bulk cells, leading to the emergent unjamming of the entire monolayer.

Conflicts of interest

There are no conflicts to declare.

Acknowledgements

SZ is supported by the ERC advanced grant 291002 SIZEEFFECTS. OC and SZ acknowledges support from the Academy of Finland FiDiPro program, project 13282993. GS is supported by Associazione Italiana per la Ricerca sul Cancro (AIRC, IG#18621), and the Italian Ministry of Health (RF-2013-02358446).

References

- 1 P. Friedl and D. Gilmour, *Nat. Rev. Mol. Cell Biol.*, 2009, **10**, 445–457.
- 2 O. Ilina and P. Friedl, *J. Cell Sci.*, 2009, **122**, 3203–3208.
- 3 D. T. Tambe, C. C. Hardin, T. E. Angelini, K. Rajendran, C. Y. Park, X. Serra-Picamal, E. H. Zhou, M. H. Zaman, J. P. Butler, D. A. Weitz, J. J. Fredberg and X. Trepat, *Nat. Mater.*, 2011, **10**, 469–475.
- 4 A. Brugues, E. Anon, V. Conte, J. H. Veldhuis, M. Gupta, J. Colombelli, J. J. Munoz, G. W. Brodland, B. Ladoux and X. Trepat, *Nat. Phys.*, 2014, **10**, 683–690.
- 5 A. Haeger, M. Krause, K. Wolf and P. Friedl, *Biochim. Biophys. Acta*, 2014, **1840**, 2386–2395.
- 6 J. R. Lange and B. Fabry, *Exp. Cell Res.*, 2013, **319**, 2418–2423.
- 7 T. M. Koch, S. Münster, N. Bonakdar, J. P. Butler and B. Fabry, *PLoS One*, 2012, **7**, e33476.
- 8 T. E. Angelini, E. Hannezo, X. Trepat, M. Marquez, J. J. Fredberg and D. A. Weitz, *Proc. Natl. Acad. Sci. U. S. A.*, 2011, **108**, 4714–4719.
- 9 J.-A. Park, J. H. Kim, D. Bi, J. A. Mitchel, N. T. Qazvini, K. Tantisira, C. Y. Park, M. McGill, S.-H. Kim, B. Gweon, J. Notbohm, R. Steward, Jr, S. Burger, S. H. Randell, A. T. Kho, D. T. Tambe, C. Hardin, S. A. Shore, E. Israel, D. A. Weitz, D. J. Tschumperlin, E. P. Henske, S. T. Weiss, M. L. Manning, J. P. Butler, J. M. Drazen and J. J. Fredberg, *Nat. Mater.*, 2015, **14**, 1040–1048.
- 10 O. Chepizhko, C. Giampietro, E. Mastrapasqua, M. Nourazar, M. Ascagni, M. Sugni, U. Fascio, L. Leggio, C. Malinverno, G. Scita, S. Santucci, M. J. Alava, S. Zapperi and C. A. M. La Porta, *Proc. Natl. Acad. Sci. U. S. A.*, 2016, **113**, 11408–11413.
- 11 A. J. Liu, S. R. Nagel and J. S. Langer, *Annu. Rev. Condens. Matter Phys.*, 2010, **1**, 347–369.
- 12 K. Doxzen, S. R. K. Vedula, M. C. Leong, H. Hirata, N. S. Gov, A. J. Kabla, B. Ladoux and C. T. Lim, *Integr. Biol.*, 2013, **5**, 1026–1035.
- 13 S. Garcia, E. Hannezo, J. Elgeti, J.-F. Joanny, P. Silberzan and N. S. Gov, *Proc. Natl. Acad. Sci. U. S. A.*, 2015, **112**, 15314–15319.
- 14 C. Malinverno, S. Corallino, F. Giavazzi, M. Bergert, Q. Li, M. Leoni, A. Disanza, E. Frittoli, A. Oldani, E. Martini, T. Lendenmann, G. Deflorian, G. V. Beznoussenko, D. Poulidakos, O. K. Haur, M. Uroz, X. Trepat, D. Parazzoli, P. Maiuri, W. Yu, A. Ferrari, R. Cerbino and G. Scita, *Nat. Mater.*, 2017, **16**, 587–596.
- 15 D. Bi, J. H. Lopez, J. M. Schwarz and M. L. Manning, *Nat. Phys.*, 2015, **11**, 1074–1079.
- 16 B. Li and S. X. Sun, *Biophys. J.*, 2014, **107**, 1532–1541.
- 17 D. Bi, X. Yang, M. C. Marchetti and M. L. Manning, *Phys. Rev. X*, 2016, **6**, 021011.
- 18 D. Weaire and J. P. Kermode, *Philos. Mag. B*, 1984, **50**, 379–395.
- 19 T. Okuzono and K. Kawasaki, *Phys. Rev. E: Stat. Phys., Plasmas, Fluids, Relat. Interdiscip. Top.*, 1995, **51**, 1246–1253.
- 20 B. Szabó, G. J. Szöllösi, B. Gönci, Z. Jurányi, D. Selmeczi and T. Vicsek, *Phys. Rev. E: Stat., Nonlinear, Soft Matter Phys.*, 2006, **74**, 061908.
- 21 M. Poujade, E. Grasland-Mongrain, A. Hertzog, J. Jouanneau, P. Chavrier, B. Ladoux, A. Buguin and P. Silberzan, *Proc. Natl. Acad. Sci. U. S. A.*, 2007, **104**, 15988–15993.
- 22 S. Henkes, Y. Fily and M. C. Marchetti, *Phys. Rev. E: Stat., Nonlinear, Soft Matter Phys.*, 2011, **84**, 040301.
- 23 N. Sepúlveda, L. Petitjean, O. Cochet, E. Grasland-Mongrain, P. Silberzan and V. Hakim, *PLoS Comput. Biol.*, 2013, **9**, e1002944.
- 24 S. R. K. Vedula, A. Ravasio, C. T. Lim and B. Ladoux, *Physiology*, 2013, **28**, 370–379.
- 25 Y. Fily, S. Henkes and M. C. Marchetti, *Soft Matter*, 2014, **10**, 2132–2140.
- 26 L. Berthier, *Phys. Rev. Lett.*, 2014, **112**, 220602.
- 27 R. Mandal, P. J. Bhuyan, M. Rao and C. Dasgupta, *Soft Matter*, 2016, **12**, 6268–6276.
- 28 G. Szamel, *Phys. Rev. E*, 2016, **93**, 012603.
- 29 E. Flenner, G. Szamel and L. Berthier, *Soft Matter*, 2016, **12**, 7136–7149.
- 30 Q. Liao and N. Xu, *Soft Matter*, 2018, **14**, 853–860.
- 31 D. L. Barton, S. Henkes, C. J. Weijer and R. Sknepnek, *PLoS Comput. Biol.*, 2017, **13**, e1005569.
- 32 V. Tarle, A. Ravasio, V. Hakim and N. S. Gov, *Integr. Biol.*, 2015, **7**, 1218–1227.
- 33 G. Balconi, R. Spagnuolo and E. Dejana, *Arterioscler., Thromb., Vasc. Biol.*, 2000, **20**, 1443–1451.
- 34 M. G. Lampugnani, A. Zanetti, F. Breviario, G. Balconi, F. Orsenigo, M. Corada, R. Spagnuolo, M. Betson, V. Braga and E. Dejana, *Mol. Biol. Cell*, 2002, **13**, 1175–1189.
- 35 C. Giampietro, A. Disanza, L. Bravi, M. Barrios-Rodiles, M. Corada, E. Frittoli, C. Savorani, M. G. Lampugnani, B. Boggetti, C. Niessen, J. L. Wrana, G. Scita and E. Dejana, *J. Cell Biol.*, 2015, **211**, 1177–1192.
- 36 W. Thielicke and E. Stamhuis, *J. Stat. Softw.*, 2014, **2**, e30.
- 37 T. Vicsek, A. Czirók, E. Ben-Jacob, I. Cohen and O. Shochet, *Phys. Rev. Lett.*, 1995, **75**, 1226–1229.
- 38 C. Maggi, U. M. B. Marconi, N. Gnan and R. Di Leonardo, *Sci. Rep.*, 2015, **5**, 10742.
- 39 T. F. F. Farage, P. Krinninger and J. M. Brader, *Phys. Rev. E: Stat., Nonlinear, Soft Matter Phys.*, 2015, **91**, 042310.
- 40 E. Fodor, C. Nardini, M. E. Cates, J. Tailleur, P. Visco and F. van Wijland, *Phys. Rev. Lett.*, 2016, **117**, 038103.
- 41 A. Zaritsky, D. Kaplan, I. Hecht, S. Natan, L. Wolf, N. S. Gov, E. Ben-Jacob and I. Tsarfaty, *PLoS Comput. Biol.*, 2014, **10**, e1003747.

- 42 A. Zaritsky, E. S. Welf, Y.-Y. Tseng, M. A. Rabadán, X. Serra-Picamal, X. Trepap and G. Danuser, *Biophys. J.*, 2015, **109**, 2492–2500.
- 43 Y. Zhang, G. Xu, R. M. Lee, Z. Zhu, J. Wu, S. Liao, G. Zhang, Y. Sun, A. Mogilner, W. Losert, T. Pan, F. Lin, Z. Xu and M. Zhao, *Cell. Mol. Life Sci.*, 2017, **74**, 3841–3850.
- 44 T. E. Angelini, E. Hannezo, X. Trepap, J. J. Fredberg and D. A. Weitz, *Phys. Rev. Lett.*, 2010, **104**, 168104.
- 45 D. A. Matoz-Fernandez, E. Agoritsas, J.-L. Barrat, E. Bertin and K. Martens, *Phys. Rev. Lett.*, 2017, **118**, 158105.
- 46 X. Trepap and J. J. Fredberg, *Trends Cell Biol.*, 2011, **21**, 638–646.